Directional Fluorescence Emission by Individual V-Antennas Explained by Mode Expansion

Dries Vercruysse,[†,‡,*] Xuezhi Zheng,[§] Yannick Sonnefraud,[∥,⊥] Niels Verellen,[†,‡] Giuliana Di Martino,[∥] Liesbet Lagae,[†,‡] Guy A. E. Vandenbosch,[§] Victor V. Moshchalkov,[‡] Stefan A. Maier,[∥] and Pol Van Dorpe[†,‡]

[†]IMEC, Kapeldreef 75, B-3001 Leuven, Belgium, [‡]INPAC and Department of Physics, KU Leuven, Celestijnenlaan 200 D, B-3001 Leuven, Belgium, [§]ESAT, Department of Electrical Engineering, Katholieke Universiteit Leuven, Leuven, Belgium, and [∥]Experimental Solid State Group, Physics Department, Imperial College London, London SW7 2AZ, U.K. [⊥]Present address: Institut Néel, CNRS UPR2940, 25 Rue des Martyrs, 38042 Grenoble, France.

ABSTRACT Specially designed plasmonic antennas can, by far-field interference of different antenna elements or a combination of multipolar antenna modes, scatter light unidirectionally, allowing for directional light control at the nanoscale. One of the most basic and compact geometries for such antennas is a nanorod with broken rotational symmetry, in the shape of the letter V. In this article, we show that these V-antennas unidirectionally scatter the emission of a local dipole source in a direction opposite the undirectional side scattering of a plane wave. Moreover, we observe high directivity, up to 6 dB, only for certain well-defined positions of the emitter relative to the antenna. By employing a rigorous eigenmode expansion analysis of the V-antenna, we fully elucidate the fundamental origin of its directional behavior. All findings are experimentally verified by measuring the radiation patterns of a scattered plane wave and the emission pattern of fluorescently doped PMMA positioned in different regions around the antenna. The fundamental interference effects revealed in the eigenmode expansion can serve as guidelines in the understanding and further development of nanoscale directional scatterers.

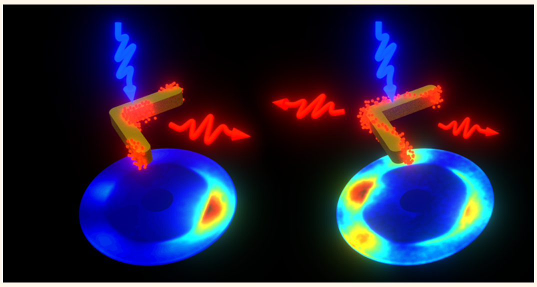

KEYWORDS: nanoantenna · surface plasmon resonance · directionality · fluorescence · eigenmode expansion · Fano resonance

Plasmonic nanoantennas form an essential tool in nano-optics, as they create a link between free-space propagating light and localized optical fields at the nanometer scale. Resonant oscillations of the free electrons in these metallic antennas, known as localized surface plasmon resonances (LSPRs), lie at the origin of their unique optical properties. Apart from their high sensitivity to the local refractive index—an effect exploited in various plasmonic sensing schemes[1]—the strong evanescent electromagnetic fields associated with LSPRs shape the optical environment, *i.e.*, the optical density of states, in the vicinity of the antenna. Because of this, emission of nanoemitters, such as fluorescent dyes,[2] quantum dots,[3] or nitrogen-vacancy color centers in diamond,[4] near these antennas depends strongly on the plasmonic modes. A large variety of plasmonic antenna shapes, such as nanorods, nanospheres, or bowtie antennas, have shown enhanced radiation as well as quenching of nearby emitters.[2,5−7] In addition to the emission decay rate, the antenna also reshapes the angular distribution of the emission from the typical Hertzian dipole angular emission pattern to more functional patterns.[8−10] Wavelength-dependent radiation patterns have, for example, been used to detect hydrogen near a bimetallic dimer or to sort emission from fluorophores in a metallic aperture.[11,12] Of course, directing radiation by itself can already improve detection efficiency. In this respect, these optical antennas form an analogue to the radio or microwave antennas that surround us today. Traditional antenna designs are therefore being transformed to the nanoscale to operate at optical frequencies. The most prominent example is the Yagi-Uda antenna: a multiparticle antenna configuration that directs the emission of a central feed by surrounding it with a series of passive scatterers.[13−17] The wavelength-dependent spacing between these elements makes Yagi-Uda antennas bulky. Smaller directional

* Address correspondence to Dries.Vercruysse@imec.be.

Received for review May 13, 2014 and accepted July 17, 2014.

Published online July 17, 2014
10.1021/nn502616k

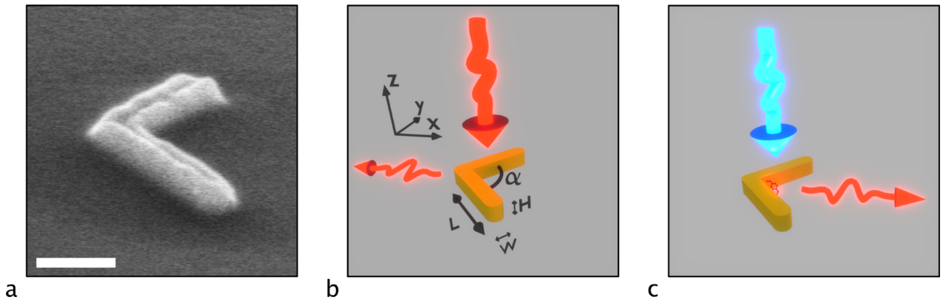

Figure 1. Radiative properties of a V-antenna: (a) SEM image of a fabricated gold V-antenna (the scale bar in the left corner is 250 nm long); (b) directional scattering of a normal-incident plane wave; (c) directional emission from an excited quantum emitter.

antenna concepts have recently appeared. However, many of them, based on nanoshells[18] or very closely spaced bars,[19] have been demonstrated only in theory due to the very specific emitter positions required and the strenuous antenna design parameters.

Recently, it was demonstrated that quantum dots covering a U-shaped split-ring resonator can emit directionally by exciting simultaneously the dipole and quadrupole antenna modes.[20] Multipolar interference was also shown to be responsible for directional cathodoluminescence emission of a simple nanosized disk.[21] Here, we will discuss in detail the interaction of a quantum emitter with a single V-shaped nanorod antenna (see SEM image in Figure 1a). In previous works, we have shown that a Fano interference between the dipole and the quadrupole-like modes of such a V-antenna can result in directional side scattering of a plane wave.[22,23] This side scattering was determined to be directed toward the V-antenna's tip, as illustrated in Figure 1b. We will show that also interference resulting from local excitation by a quantum emitter leads to directional emission. In contrast to the plane wave case, however, the emission is directed toward the antenna's opening, as illustrated in Figure 1c. Using a rigorous eigenmode expansion method (EEM),[24] it is revealed that the observed directionality in this case originates from the interference between the inherent weak directionality of the asymmetric quadrupole-like eigenmode and the uncoupled radiation emitted by the local excitation source.

Furthermore, the directivity—defined as the ratio of the power emitted in the direction of the antenna's tip and opening—is found to be strongly dependent on the emitter's position relative to the antenna. We experimentally demonstrate this directional emission by using fluorescent molecules as local excitation source. With electron beam lithography of dye-doped PMMA resist, these fluorescent molecules are positioned in specific regions around the antenna to demonstrate the position dependence and to optimize the directional emission mediated by a V-antenna on a glass substrate (Figure 1a). The emission patterns of the PMMA-covered antennas are measured by back focal plane (BFP) imaging and found to be in excellent agreement with EEM and finite difference time domain (FDTD) simulation results.

EIGENMODE ANALYSIS

A charge oscillation excited in a plasmonic antenna is typically a superposition of several plasmonic modes. The charge distribution of these modes depends on the antenna's geometry, while the intensity and phase at which these modes contribute to the total charge oscillation depend on the excitation source and can be described by complex coupling coefficients. The modes of an antenna, as well as the coupling coefficients, can be found by an eigenmode expansion. We use an in-house-developed computational software, MAGMAS, which is based on a Volumetric Method of Moments algorithm,[25−32] to extract the eigenmodes and their coupling coefficients to a specific excitation (see methods in the Supporting Information). Eigenmode expansions for wavelengths between 600 and 1300 nm are done for an antenna with an arm length $L = 300$ nm, width $W = 42$ nm, height $H = 50$ nm, and an angle $\alpha = 90°$ between the arms, as indicated in Figure 1b. Figure 2b shows the five lowest order V-antenna eigenmodes at $\lambda = 694$ nm, the top surface charge distributions (orange and green are positive and negative charge, respectively), and the corresponding 3D radiation patterns. The mode index, l, is defined by the number of nodes in the charge distribution.

The radiation fields as well as the charge distributions are complex quantities. The phase of the electrical field at the *xy*-plane is shown in blue/red-scale below the 3D radiation patterns, plotted on the *z*-axis along the 2D-cut (black line) of the radiation pattern. Panel a in Figure 2 illustrates how the phase of the electric field in spherical coordinates needs to be interpreted. In the far field on the *xy*-plane the only component present will be along the ϕ unit vector, $\bar{e}_\phi$, shown in black. Using this coordinate system, the radiation's phase of a dipole mode at opposite sides will show a π phase difference. The electric field at both

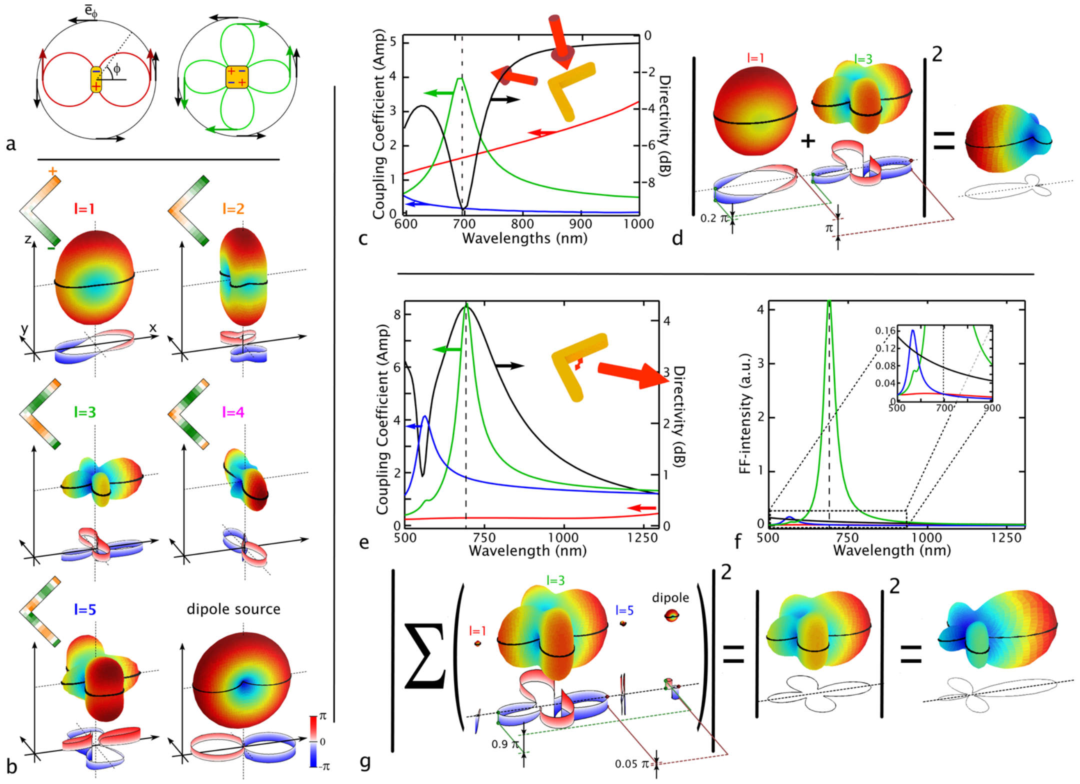

Figure 2. Eigenmode analysis of the V-antenna. (a) 2D radiation patterns of a dipole (left) and quadrupole (right). (b) 3D radiation patterns ($|E|^2$) and charge density plots (top left corners) of the five lowest order plasmonic eigenmodes at $\lambda_{l=3}$. The phase of the light emitted at the *xy*-plane is plotted on the *z*-axis on the *xy*-cut from the radiation plots. Lower-right figure depicts the excitation point dipole source located in the center as indicated in the inset of panel e. (c, d) Eigenmode decomposition in the case of normal-incident plane wave excitation. (c) Coupling factor amplitudes for $l = 1$ (red), $l = 3$ (green), and $l = 5$ (blue) modes, and plane wave scattering directivity (black, right axis). (d) 3D patterns of the field amplitude ($\sqrt{|E|^2}$) and phase for the $l = 1$ and $l = 3$ modes and the summed power scattering plot at $\lambda_{l=3}$. (e−g) Eigenmode decomposition in the case of excitation by a centrally positioned *y*-polarized point dipole source (indicated with the red dipole in the inset in e). (e) Coupling factor amplitudes for $l = 1$ (red), $l = 3$ (green), and $l = 5$ (blue), and dipole emission directivity (black, right axis). (f) Power emitted to the far-field (FF) as a function of the wavelength for each mode and for the uncoupled dipole emission in black. (g) 3D radiation patterns of the field and the phase of the $l = 1$, 3, and 5 modes, the uncoupled dipole source emission, and the summed field and power scattering plots at $\lambda_{l=3}$.

sides points in the same direction, while $\bar{e}_\phi$ flips direction, as can be seen in the right 2D scatter pattern. The first-order mode, $l = 1$, in panel b clearly shows the π phase difference. The phase of this dipole mode is positive in the positive *x*-direction and negative in the opposite direction. Other modes with a net dipole, $l = 2$ and $l = 4$, show the same π difference. A quadrupole mode is depicted at the right in panel a. In this case the direction of the electric field in opposing lobes changes direction, just as $\bar{e}_\phi$ does. Because of this, the phase in the positive and negative direction along the axes will be the same. The $l = 3$ mode in panel b has a quadrupolar character and thus shows very little phase difference in opposing directions. Interestingly, the radiation pattern of $l = 3$ presents a certain directionality in the *x*-direction. Due to reduced symmetry of the antenna, the extracted eigenmode's charge oscillation deviates from a purely symmetric Mie quadrupole, hence enabling the observed modal directivity. The spectral dependence of the $l = 3$ mode's directivity is shown in Figure S3 in the Supporting Information. At the eigenmode wavelength, $\lambda_{l=3}$, where the coupling coefficient of the $l = 3$ eigenmode reaches its maximum, the directivity of the eigenmode itself—the modal directivity—reaches 1.5 dB. The directivity is defined as $10 \times \log_{10}(P_r/P_l)$, with P_r the power radiated right along the positive *x*-direction (antenna opening) and P_l the power radiated left along the negative *x*-direction (antenna tip).

After characterizing the V-antenna's eigenmodes in Figure 2b, we now consider two specific excitation sources for which the coupling coefficients and radiation patterns are calculated: a normal-incident plane wave (Figure 2c,d) and a point dipole source (Figure 2e−g).

For the *y*-polarized plane wave excitation, the coupling coefficients of the $l = 1$, 3, and 5 modes around $\lambda_{l=3}$, shown in Figure 2c, indicate that mainly the $l = 1$ (red curve) and $l = 3$ (green curve) eigenmodes contribute to the plasmonic oscillation, as $l = 5$ (blue curve) is only very weakly excited. To reveal how these modes interfere in the far-field, we evaluate the complex electrical fields rather than the power. In Figure 2d, the electric field amplitude scattering plots ($\sqrt{|E|^2}$) for the l = 1 and l = 3 eigenmodes, taking into account the complex coupling coefficients, *i.e.*, their individual amplitude and relative phase in the eigenmode decomposition, are shown. The corresponding phase plots clearly show that, in the negative *x*-direction, light radiated by the $l = 3$ eigenmode is almost in-phase with the $l = 1$ eigenmode. For the positive *x*-direction, on the other hand, both modes radiate with a phase difference close to π. The modes, hence, interfere destructively in the positive *x*-direction, reducing the l = 3 eigenmode's modal main lobe to the right, while constructively in the negative *x*-direction, enhancing the modal back lobe (*i.e.*, the lobe opposing the main lobe). This interference gives rise to the negative directivity (main lobe in negative *x*-direction) of -9 dB observed in Figure 2c (black curve, right axis). Note that this directivity strongly exceeds the third-order eigenmode's modal weak directivity of only 1.5 dB. The resulting power scattering plot ($|E|^2$) is shown in Figure 2d.

For the local excitation by a point dipole source polarized along the *y*-axis and located at the center of the antenna, a similar analysis is made. Figure 2e shows the resulting coupling coefficients of the l = 1, 3, and 5 modes around $\lambda_{l=3}$. At this wavelength, the dipole source excites both the $l = 3$ and $l = 5$ modes, while it barely couples to the $l = 1$ mode. To evaluate a mode's contribution to the far-field radiation intensity, however, coupling factors are not ideal since not all modes are equally radiative and since it does not give the contribution of the uncoupled light coming from the emitter. Therefore, in Figure 2f we show the power sent by each mode into the far-field. The $l = 3$ mode (green curve) is clearly the dominant contribution. Nevertheless, the modal directivity of 1.5 dB for this eigenmode does not account for the >4 dB directivity that is observed in panel e (black curve, right axis). When zooming-in on $l = 3$ in panel f (inset), it turns out that the light from the excitation source that does not couple to the antenna has a non-negligible far-field contribution, as shown by the black curve in Figure 2f. To assess how all these far-field contributions compare and interfere, the scattering plots of the field amplitude ($\sqrt{|E|^2}$) at $\lambda_{l=3}$ are shown in Figure 2g. As already seen in panel f, modes l = 1 and 5 are very weak. The uncoupled dipole source light on the other hand, albeit smaller than the $l = 3$ mode, is not negligible. The corresponding phase shows that the uncoupled light and the $l = 3$ mode interfere constructively in the positive while destructively in the negative *x*-direction. By diminishing the already smaller back lobe of the $l = 3$ eigenmode, this explains the increase in directivity from 1.5 to 4 dB, despite the limited amplitude of the uncoupled light.

The coupling efficiency of an emitter to a specific nanoantenna mode is determined by the mode's optical density of states and, hence, strongly depends on the near-field intensity at the location of the emitter. Consequently, it is expected that the coupling coefficients (~phase and amplitude of the excited modes) will depend on the exact position (and polarization) of the emitter. Therefore, different radiation patterns should appear when the dipole source is moved around the V-antenna. In order to get a complete picture of how the dipole source position influences the emission properties, a series of FDTD simulations were performed. From these simulations the emission rates and far-field emission patterns of a dipole source at different locations around a rounded V-antenna are derived. Taking symmetry into account, the positions of only one quadrant of the antenna, indicated by purple dots in Figure 3a, need to be simulated. Experimentally, the orientation of a fluorescent molecule cannot be controlled. To include this random orientation, three simulations are performed at every position, each with a different polarization of the dipole: one perpendicular and two parallel to the antenna surface, as illustrated in panel a. On the basis of these simulations various properties of the emitter can be mapped along the antenna's surface. Panel b and c of Figure 3 show, respectively, the enhancement at $\lambda_{l=3}$ of the nonradiative (Γ_{nr}/Γ_0) and radiative (Γ_r/Γ_0) decay rates, with Γ_0 the decay rate of the dipole source in free space and $\Gamma_{nr,r}$ the decay rates in the presence of the antenna. The highest nonradiative and radiative decay rates are typically seen on the inside of the V-shape between the two arms (red regions). However, in addition, the tips of the antenna seem to contribute to the emission as well (panel c). A similar map of the quantum efficiency, based on these decay rates, $\Gamma_r/(\Gamma_{nr} + \Gamma_r)$, can be found in the Supporting Information (Figure S4). From the far-field projections of these simulations we obtain information on the direction and polarization of the emitted light. Panel e shows the directivity over the antenna surface. From this plot, four different regions, which are indicated in Figure 3d, can be assigned to the arm of the antenna. We will refer to them as the inside top, outside top, inside center, and outside center regions. The center region (red region in panel e) is clearly the best position for an emitter to get directional emission. However, it should be noted that the maximum directivity is not obtained at the connection point of the legs, *i.e.*, the emitter position discussed in Figure 2e−g, but rather at about half of the leg length from the center, *i.e.*, the position indicated in the inset of the top graph in panel f. At the tips of the V-antenna, the half at the outside of the tip (top outside) leads to directional emission, while the part at the inside (top inside) does not. The outside top and the center inside regions of the antenna are the most favorable positions for directional emission.

In the same manner as for the dipole source positioned in the center, an eigenmode expansion can explain why the emission is, or is not, directional for

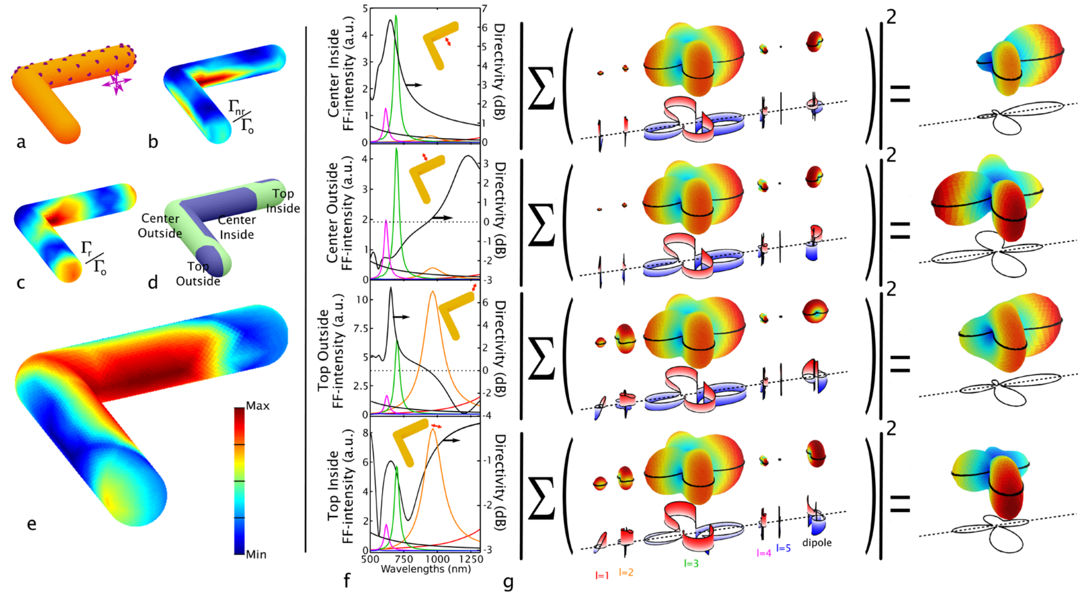

Figure 3. Position-dependent properties around the V-antenna: (a) Positions of dipoles simulated with FDTD around the rounded V-antenna at 10 nm from the antenna surface; (b) nonradiative enhancement compared to a free space emitter ([min, max] = [8,73]); (c) radiative enhancement ([min,max] = [1,29]) interpolated on the V-antenna; (d) schematic representation of the different regions on the V-antenna; (e) directivity interpolated on the V-antenna ([min,max] = [−1.8,4.2] dB); (f) power emitted to the far-field as a function of the wavelength for every mode and for the uncoupled dipole emission and the directivity on the right axis in black. The color of the curve for the different modes matches the colors in Figure 2b. (g) 3D patterns of the field ($\sqrt{|E|^2}$) and the phase at the *xy*-plane of the l = 1, 2, 3, 4, and 5 mode and the uncoupled dipole and the summed power scattering plot.

these different regions. A decomposition is done for a dipole excitation in the center of each of the four regions, as shown in the insets of panel f in Figure 3. The dipole orientation is chosen perpendicular to the surface in all four regions since this orientation has the strongest coupling. The power radiated into the far-field by the different eigenmodes and by the uncoupled source light, as well as the directivity, is shown in Figure 3f. The field scattering patterns of the modes and total power scattering pattern are shown in panel g. The loss of symmetry in the *y*-direction by moving the dipole source off-center leads to the excitation of the even-parity modes l = 2 (magenta) and 4 (orange), in addition to l = 1, 3, and 5. Although these even modes can have a strong effect on the total far-field pattern, their emission in the *x*-direction is negligible due to the symmetry of their charge oscillations, as is clearly seen in the radiation patterns of Figure 2b. Not taking these even modes into account, panel f shows for all four positions that the uncoupled dipole emission around $\lambda_{l=3}$ is still the second largest contribution after the l = 3 mode. For the two cases where the dipole is positioned halfway on the antenna's arm, the top two rows in panels f and g, the intensity with which the modes are excited is similar. Both positions easily excite l = 3 and 4, while l = 1, 2, and 5 are hardly excited. The phases on the other hand are very different. The dipole source located on the inside center interferes constructively with the main lobe of the l = 3 mode, while the dipole source located on the outside center interferes destructively with the main lobe and, additionally, constructively with the back lobe. The interference at the inside center thus enhances the modal directivity of l = 3, whereas at the outside center the interference opposes it. Since the contribution of uncoupled light is smaller than that of l = 3, the interference that destructively interferes with the smallest lobe of l = 3 will result in the highest directivity. The inside center, where this is the case, thus shows a higher directivity than the outside center, where the directivity barely reaches −2 dB.

The two bottom rows in panel f and g of Figure 3 display the different modal contributions of a plasmonic oscillation excited by a dipole at the top of the antenna's arm. The dipole source at the outside top easily excites almost all modes. Panel g shows that at this location the uncoupled dipole source radiation interferes constructively with the main lobe of l = 3, the same way as for the inside center. However, the directivity seen in the total power scattering plot on the right of panel g is lower compared to the inside center. The more pronounced presence of l = 1 is the cause of this. The l = 1 mode constructively interferes with the back lobe and destructively with the main lobe of l = 3, lowering the directivity in the positive *x*-direction. This effect is even more pronounced at the inside top, where the directivity nearly vanishes. Due to the orientation of the uncoupled dipole radiation, parallel to the *x*-axis, it does not contribute to interference in the *x*-direction. Hence, the l = 1 mode constitutes the most important interference contribution. In the same manner as for the outside top, interference of $l = 1$ with $l = 3$ enhances the back lobe of $l = 3$, lowering the directivity to −1 dB.

RESULTS AND DISCUSSION

To experimentally demonstrate the directional emission behaviors revealed in the simulations presented in Figures 2 and 3, arrays of gold V-antennas with different arm lengths L and arm opening angles α were fabricated using e-beam lithography on a glass substrate with a 15 nm ITO layer.[22] A second e-beam step was subsequently applied to pattern PMMA resist doped with fluorescent Atto 740 dye around the antennas (see Methods). Precise placement of fluorescent dye allows us to exploit and investigate the position dependency of the directivity experimentally.

The experimental results for the $L = 240$ nm, $\alpha = 90$ V-antenna covered by doped PMMA at the regions for which high directionality is expected from the analysis in Figure 3 (the outside top and the inside center) are summarized in Figure 4. Radiation patterns generated by the antenna arrays were measured by back focal plane imaging, which shows the radiation intensity in every direction toward the substrate, as schematically illustrated in Figure 4b for plane wave scattering and in panel c for fluorescence emission (see Methods for details). The spectral dependence of the directivity of the Rayleigh scattered light from a normal incident plane wave is shown by the black curve in panel a. As expected from our previous work,[22] a strong directivity up to −14 dB is observed on the longer wavelength side of the $l = 3$ extinction resonance (green curve in panel a). The latter was measured using a Fourier transform infrared (FTIR) spectrometer. The BFP image corresponding to the directivity peak is shown in the illustration in panel b. In full agreement with the simulations in Figure 2c, the plane wave light is scattered in the negative x-direction, the direction of the tip of the V-antenna.[22] The experimental directivity is calculated by integrating a small window in the BFP image around the main peak for P_r and by integrating the same mirrored window for P_l.[22]

The photoluminescence (PL) spectrum of the doped PMMA, obtained with 640 nm laser excitation, in the absence of an antenna, is shown by the dashed red line in Figure 4a. Due to the Purcell effect, this dye emission spectrum will be modified when in the proximity of a plasmonic antenna, as is seen by the blue curve in Figure 4a, which shows the PL spectrum with a V-antenna. The PL peak is located at $\lambda = 762$ nm, at a slightly longer wavelength than the 750 nm extinction maximum (green curve). This is as expected for the $l = 3$ Fano resonance, for which the maximum field enhancement is reached in the longer wavelength tail of the extinction resonance.[33,34] The experimental BFP image of the dye emission can be seen in the illustration in panel c. The blue arrow represents the excitation light. The spectral detection window in the experiment is fixed to 750−800 nm (red area in panel a), which, for the antenna with 240 nm arm length, overlaps very well with the emission enhancement. The BFP measurement clearly shows that most of the light is emitted to the right in the positive x-direction, where the PL reaches a directivity of just over 5 dB. This value corresponds well with the directivity found in the simulation in Figure 2e. To reduce the background signal in the BFP images, the PL signal was filtered with a polarizer to only show the y-polarized light. A BFP image without the polarization filter and of plain PMMA can be found in the Supporting Information, Figure S6.

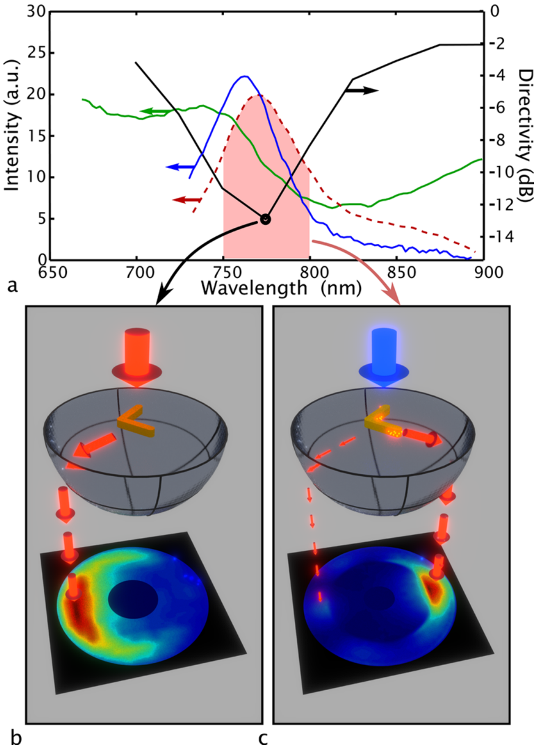

Figure 4. Experimental directivity measurements. (a) Spectra of an array of V-antennas with $L = 240$ nm and $\alpha = 90°$: extinction spectra (green), scattering directivity (black, right axis), and PL spectrum of V-antenna covered with doped PMMA (blue). The dashed red line shows the PL of Atto 740 doped PMMA. The filled area indicates the spectral window that passes by the camera. (b) Schematic illustration of light scattered by a V-antenna on a glass substrate. (c) Schematic illustration of light emitted by well-positioned dyes near the V-antenna on a glass substrate. Both b and c show how the light is projected in a BFP image.

In order to obtain spectral information, rather than using different dye with different emission spectra, the arm length of the antenna is varied, while the spectral detection window is fixed to 750−800 nm. Increasing the arm length red-shifts the antenna's modes, causing a different part of the $l = 3$ Fano resonance to overlap with the dye's photoluminescence spectrum. Figure S5 shows how the $l = 3$ resonance shifts within the PL spectra of V-antennas with arm lengths varying from

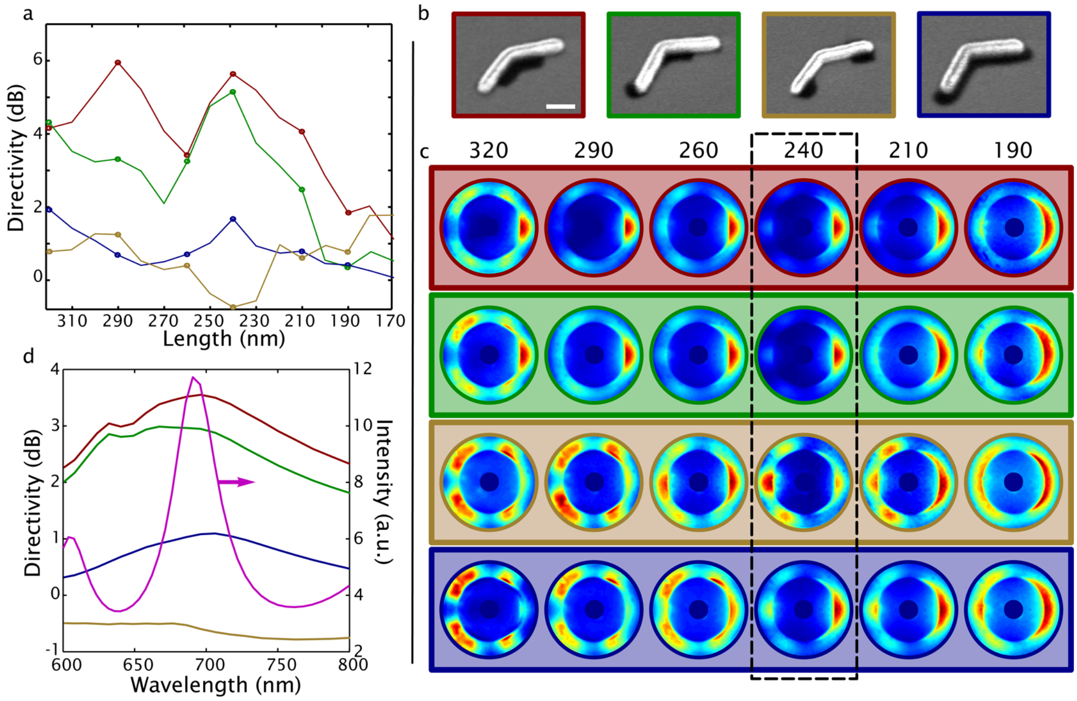

Figure 5. Experimental measurements for different PMMA patterns. (a) Directivity as a function of the arm length for PMMA patterns that cover the entire antenna (blue), only outside top and the inside center (green), only the inside center (red), and the outside center and the inside top (brown). (b) SEM images of V-antennas with different PMMA patterns. The large angle ($\alpha = 150°$) of these antennas helps to visualize the PMMA; however the antennas discussed in a, c, and d all have a 90° angle. The scale bar in the left panel is 125 nm long. (c) BPF measurements of the V-antennas with the different PMMA patterns and varying arm length. The colors of the frame match the colors of panel a. (d) FDTD-simulated directivity for the different PMMA patterns and the total far-field intensity in purple on the right axis. The colors of the curves match the colors of panel a.

220 to 300 nm. The directivity as a function of the arm length for the antenna with PMMA in the directional regions, as in Figure 4c, is shown by the green curve in Figure 5a. A clear maximum is observed for the antenna with a length of $L = 240$ nm, whose Fano resonance overlaps with the spectral detection window (Figure 4a). The BFP images for the arm lengths indicated by dots in Figure 5a are shown in panel c (green box). Figure 5d shows the directivity spectrum obtained from FDTD simulations. The simulated antenna has its $l = 3$ resonance around 700 nm, as is revealed from the total far-field intensity spectrum (purple curve). The directivity in this figure is obtained by summing the far-field scattering plots obtained from the dipole source simulations in Figure 3a for which the source location lies in the regions corresponding to the PMMA pattern. The directivity clearly peaks at the $l = 3$ resonance, reaching a value of 3 dB in the simulations, while even reaching 5 dB experimentally.

In addition to the placement of doped PMMA in the directional regions, three more PMMA patterns on the V-antenna are tested. Figure 5b shows SEM images of the four different patterns, where the darker regions indicate the presence of PMMA. From left to right: an antenna with dye only in the inside center (red), only in the directional regions (green), only in the inside top and the outside center (brown) [the green regions indicated in Figure 3d, which do not generate high directionality], and a fully covered antenna (blue). The directivity as a function of the arm length for these additional PMMA patterns is included in Figure 5a, and the BFP images for the arm lengths indicated by dots are shown in panel c. The corresponding FDTD simulation results are shown in panel d. Like in the simulations, the experiments show the highest directivity for the PMMA pattern that covers only the inside center (red). In the experiments for the center PMMA coverage, a second peak appears at $L = 290$ nm next to the peak where the $l = 3$ resonance overlaps with the 750–800 nm window. This peak can be seen in the FDTD simulation results as well, although it is much less pronounced. The directivity spectra of the eigenmode expansion in Figure 3 show that for the central inside and top inside placement the highest directionality is actually seen on the blue side of the $l = 3$ resonance. Yet, as the simulated PL spectrum in Figure 5d (purple curve) indicates, the PL is very low at the second directivity peak. This explains why this second directivity peak is not experimentally observed for the PMMA pattern with the top outside included in the pattern (green). Indeed, this region couples less efficiently to the $l = 3$ mode, creating more background emission, which lowers the directionality. This background emission is visible in Figure 5c for $L = 290$ nm. The brown line in Figure 5a shows the directivity of the PMMA pattern combining the inside top and center outside. Here, dyes are positioned where they should not contribute to the directivity toward the positive *x*-direction. The directivity varies around 0 dB, reaching a minimum of almost −1 dB at *L* = 240 nm. Although the BFP measurements for this coverage show the same lobes as the previous PMMA patterns, indicating interaction with the same modes, the intensity of the different lobes is very similar, resulting in limited directionality. The directivity of a fully covered antenna (blue line in panel a) has, as expected from the simulation in panel d, only a small maximum, barely reaching 2 dB, which appears around *L* = 240 nm. Knowing that the green and brown PMMA patterns in panel b combined form the full coverage pattern (blue), it is seen that for the smaller antennas up to 240 nm the directional dye placement of the green pattern dominates the blue BFP images. For the larger antennas, on the other hand, the undirectional brown pattern seems to dominate.

All previously discussed antennas are bent at an angle of α = 90°. Figure S7 shows the directivity of V-antennas with *L* = 240 nm and varying α from 90° to 180° for the different tested PMMA patterns. The directionality of the full, directional, and center coverage reaches its maximum at α = 90° and gradually decreases toward nearly 0 dB at α = 180°. As expected, all BPF images for the different PMMA pattern shown in Figure S7b converge to the typical emission pattern of the *l* = 3 mode of a nanorod (α = 180°).[9] This indicates that symmetry breaking by positioning the local emitter off-center is not sufficient to obtain directional behavior (*e.g.*, not a mirror effect) and that therefore the radiation properties of the coupled antenna modes, which are directly related to the charge oscillation distribution, play a crucial role.

CONCLUSIONS

In conclusion, we have demonstrated that the omnidirectional emission of a quantum emitter can be redirected in a specific direction by placing it in close proximity to a V-shaped metallic nanorod antenna. Using a newly developed eigenmode expansion method, it was revealed that the unidirectional emission mostly arises from an interference of the quadrupolar *l* = 3 antenna mode and the uncoupled radiation of the emitter. Since this uncoupled radiation intensity is generally weak compared to the antenna radiation, high directivity is observed only for specific positions of the emission source where the interference enhances the modal directivity of the *l* = 3 mode. By placing fluorescent molecules at these positions—extracted from a full, simulated directivity map of the antenna—we experimentally observed directivity values reaching 6 dB. Interestingly, the emission occurs in opposite direction of the unidirectionally Rayleigh scattered light of a plane wave in the same spectral window. Eigenmode analysis revealed that here, unlike for the emission, the directional behavior is dominated by interference of the quadrupolar *l* = 3 and dipolar *l* = 1 antennas' modes. The directivity disappeared when the fluorescent dye was positioned in locations for which simulations predicted no directional behavior. Additionally, when the geometrical asymmetry of the V-antenna is removed, resulting in an axially symmetric nanorod, no directional behavior is observed either. The obtained insight in how directional emission and scattering are generated and how different modes come together to form far-field properties of a plasmonic device is indispensable to create new nanoscale optical devices as well as to improve existing ones.

METHODS

Sample Fabrication. The antennas are fabricated on a glass microscope slide coated with 15 nm of indium tin oxide (ITO). The conductive ITO layer is necessary for the second electron beam lithography (EBL) step and facilitates SEM inspection of the sample. After sputtering 50 nm gold (the antenna height) on the slides, the antenna shape is patterned on top using EBL with negative tone hydrogen silsesquioxane resist. The unpatterned gold is removed by Xe ion milling, after which the remaining resist on top of the antennas is removed with a sulfur hexafluoride and oxygen dry etch (Oxford Instruments Plasmalab System 100 ICP 180).[35] The antennas are arranged in two sets of arrays of 40 by 50 μm with a pitch of 2 and 4.5 μm, respectively. All but the BFP scattering measurements are done on the 2 μm pitch arrays. After the antennas are fabricated, fluorescently doped PMMA is patterned on top. For this, Atto 740 dye dissolved in dimethoxyethanol is mixed with PMMA in the same solvent and spin coated on the sample, forming a 30 nm thick film, and baked for 5 min at 90 °C. In a second e-beam illumination and development all the unwanted PMMA around the antenna is removed. The sample subsequently receives an oxygen plasma treatment for 3 s to remove residual dye. The alignment error between the two e-beam steps is typically below 10 nm.

Experimental Setup for Optical Measurements. Extinction (1 − transmission) spectra are taken with a Fourier transform infrared microscope (Bruker vertex 80v + Hyperion) using two 15× magnification Cassegrain condensers. The photoluminescence signal of the covered antennas is measured using a microscope with a 20× oil immersion objective (NA = 0.91). Picosecond pulsed laser light of a Ti:sapphire laser is focused to a 20 μm spot on the antenna array. The PL signal from this spot is then sent to a spectrometer equipped with a Si CCD camera. Both the linear laser scattering and the dye emission angular distribution are measured using back focal plane imaging. For the linear scattering, monochromatic light, selected from a supercontinuum laser source using a prism, is passed through a polarizer and focused on the sample by a low NA objective. A 100× magnification oil immersion objective with an NA of 1.49 collects the scattered and transmitted light from the sample. Two lenses project the BFP of this high NA objective on an opaque disk, which blocks the bright central spot generated by the unscattered light. This filtered image is subsequently transferred to a CCD camera.[16,22,36] Since the antennas are arranged in a grid, the BFP shows an regular interference grid superimposed on the single antenna response. Values in between the interference maxima were interpolated to produce a smoother image as in ref 22. For the photoluminescence BFP measurements, the same optical path is used. A 640 nm picosecond pulsed laser (Picoquant LDH-D-C-640) is used as the excitation source, which is filtered away from the detection path by a dichroic at 750 nm. In addition, the collected PL light passes an

800 nm short pass filter in order to remove the secondary fluorescence peak at 850 nm, leaving a 50 nm wide spectral detection window. Detailed schematic drawings of the setup can be found in the Supporting Information, Figure S1.

Conflict of Interest: The authors declare no competing financial interest.

Acknowledgment. D.V. acknowledges the I.W.T. Flanders and N.V. the FWO Flanders for financial support. N.V. and V.V.M. are supported by the Methusalem funding by the Flemish Government. The authors thank Jos Moonens and Josine Loo for e-beam assistance. Y.S. and S.A.M. acknowledge support from the EPSRC and the Leverhulme Trust.

Supporting Information Available: Additional information about the setup and the eigenmode decomposition as well as extra figures of the simulated directivity of the $l = 3$ mode, the quantum efficiency at $\lambda_{l=3}$, the photoluminescence spectra, and the back focal plane images without a polarization filter and without antennas and of V-antennas with different angles are available free of charge *via* the Internet at http://pubs.acs.org.

REFERENCES AND NOTES

1. Mayer, K. M.; Hafner, J. H. Localized Surface Plasmon Resonance Sensors. *Chem. Rev.* **2011**, *111*, 3828–3857.
2. Cheng, Y.; Stakenborg, T.; Van Dorpe, P.; Lagae, L.; Wang, M.; Chen, H.; Borghs, G. Fluorescence Near Gold Nanoparticles for DNA Sensing. *Anal. Chem.* **2011**, *83*, 1307–1314.
3. Tanaka, K.; Plum, E.; Ou, J. Y.; Uchino, T.; Zheludev, N. I. Multifold Enhancement of Quantum Dot Luminescence in Plasmonic Metamaterials. *Appl. Phys. Lett.* **2010**, *105*, 227403.
4. Lončar, M.; Faraon, A. Quantum Photonic Networks in Diamond. *MRS Bull.* **2013**, *38*, 144–148.
5. Lu, G.; Li, W.; Zhang, T.; Yue, S.; Liu, J.; Hou, L.; Li, Z.; Gong, Q. Plasmonic-Enhanced Molecular Fluorescence within Isolated Bowtie Nano-Apertures. *ACS Nano* **2012**, *6*, 1438–1448.
6. Kajetan Schmidt, M.; Mackowski, S.; Aizpurua, J. Control of Single Emitter Radiation by Polarization-and Position-Dependent Activation of Dark Antenna Modes. *Opt. Lett.* **2012**, *37*, 1017–1019.
7. Anger, P.; Bharadwaj, P.; Novotny, L. Enhancement and Quenching of Single-Molecule Fluorescence. *Appl. Phys. Lett.* **2006**, *96*, 113002.
8. Taminiau, T. H.; Stefani, F. D.; van Hulst, N. F. Optical Nanorod Antennas Modeled as Cavities for Dipolar Emitters: Evolution of Sub- and Super-Radiant Modes. *Nano Lett.* **2011**, *11*, 1020–1024.
9. Curto, A. G.; Taminiau, T. H.; Volpe, G.; Kreuzer, M. P.; Quidant, R.; van Hulst, N. F. Multipolar Radiation of Quantum Emitters with Nanowire Optical Antennas. *Nat. Commun.* **2013**, *4*, 1750.
10. Koenderink, A. F. Plasmon Nanoparticle Array Waveguides for Single Photon and Single Plasmon Sources. *Nano Lett.* **2009**, *9*, 4228–4233.
11. Shegai, T.; Johansson, P.; Langhammer, C.; Käll, M. Directional Scattering and Hydrogen Sensing by Bimetallic Pd−Au Nanoantennas. *Nano Lett.* **2012**, *12*, 2464–2469.
12. Aouani, H.; Mahboub, O.; Devaux, E.; Rigneault, H.; Ebbesen, T. W.; Wenger, J. Plasmonic Antennas for Directional Sorting of Fluorescence Emission. *Nano Lett.* **2011**, *11*, 2400–2406.
13. Maksymov, I. S.; Staude, I.; Miroshnichenko, A. E.; Kivshar, Y. S. Optical Yagi-Uda Nanoantennas. *Nanophotonics* **2012**, *1*, 65–81.
14. Kosako, T.; Kadoya, Y.; Hofmann, H. F. Directional Control of Light by a Nano-Optical Yagi−Uda Antenna. *Nat. Photonics* **2010**, *4*, 312–315.
15. Dregely, D.; Taubert, R.; Dorfmüller, J.; Vogelgesang, R.; Kern, K.; Giessen, H. 3D Optical Yagi-Uda Nanoantenna Array. *Nat. Commun.* **2011**, *2*, 267.
16. Curto, A. G.; Volpe, G.; Taminiau, T. H.; Kreuzer, M. P.; Quidant, R.; van Hulst, N. F. Unidirectional Emission of a Quantum Dot Coupled to a Nanoantenna. *Science* **2010**, *329*, 930–933.
17. Taminiau, T. H.; Stefani, F. D.; van Hulst, N. F. Enhanced Directional Excitation and Emission of Single Emitters by a Nano-optical Yagi-Uda antenna. *Opt. Express* **2008**, *16*, 10858–10856.
18. Pellegrini, G.; Mazzoldi, P.; Mattei, G. Asymmetric Plasmonic Nanoshells as Subwavelength Directional Nanoantennas and Color Nanorouters: A Multipole Interference Approach. *J. Phys. Chem. C* **2012**, *116*, 21536–21546.
19. Pakizeh, T.; Käll, M. Unidirectional Ultracompact Optical Nanoantennas. *Nano Lett.* **2009**, *9*, 2343–2349.
20. Hancu, I. M.; Curto, A. G.; Castro-López, M.; Kuttge, M.; van Hulst, N. F. Multipolar Interference for Directed Light Emission. *Nano Lett.* **2013**, *14*, 166–171.
21. Coenen, T.; Arango, F. B.; Koenderink, A. F.; Polman, A. Directional Emission from a Single Plasmonic Scatterer. *Nat. Commun.* **2014**, *5*, 3250.
22. Vercruysse, D.; Sonnefraud, Y.; Verellen, N.; Fuchs, F. B.; Di Martino, G.; Lagae, L.; Moshchalkov, V. V.; Maier, S. A.; Van Dorpe, P. Unidirectional Side Scattering of Light by a Single-Element Nanoantenna. *Nano Lett.* **2013**, *13*, 3843–3849.
23. Verellen, N.; López-Tejeira, F.; Paniagua-Domínguez, R.; Vercruysse, D.; Denkova, D.; Lagae, L.; Van Dorpe, P.; Moshchalkov, V. V.; Sánchez-Gil, J. A. Mode Parity-Controlled Fano- and Lorentz-like Line Shapes Arising in Plasmonic Nanorods. *Nano Lett.* **2014**, *14*, 2322–2329.
24. Baum, C. E. Emerging Technology for Transient and Broad-Band Analysis and Synthesis of Antennas and Scatterers. *Proc. IEEE* **1976**, *64*, 1598−1616.
25. Harrington, R. F. *Field Computation by Moments Methods*; IEEE Press, 1993.
26. Vandenbosch, G. A. E.; Van de Capelle, A. R. Mixed-Potential Integral Expression Formulation of the Electric Field in a Stratified Dielectric Medium-Application to the Case of a Probe Current Source. *IEEE Trans. Antennas Propag.* **1992**, *40*, 806−817.
27. Demuynck, F. J.; Vandenbosch, G. A. E.; Van de Capelle, A. R. The Expansion Wave Concept. I. Efficient Calculation of Spatial Green's Functions in a Stratified Dielectric Medium. *IEEE Trans. Antennas Propag.* **1998**, *46*, 397–406.
28. Vandenbosch, G. A. E.; Demuynck, F. J. The Expansion Wave Concept. ii. A New Way to Model Mutual Coupling in Microstrip Arrays. *IEEE Trans. Antennas Propag.* **1998**, *46*, 407–413.
29. Vrancken, M.; Vandenbosch, G. A. E. Hybrid Dyadic-Mixed-Potential and Combined Spectral-Space Domain Integral-Equation Analysis of Quasi-3-d Structures in Stratified Media. *IEEE Trans. Microwave Theory Technol.* **2003**, *51*, 216–225.
30. Schols, Y.; Vandenbosch, G. A. E. Separation of Horizontal and Vertical Dependencies in a Surface/Volume Integral Equation Approach to Model Quasi 3-d Structures in Multilayered Media. *IEEE Trans. Antennas Propag.* **2007**, *55*, 1086–1094.
31. Vandenbosch, G. A. E.; Volski, V.; Verellen, N.; , Moshchalkov, V. V. On the Use of the Method of Moments in Plasmonic Applications. *Radio Sci.* **2011**, *46*, RS0E02.
32. Zheng, X.; Valev, V. K.; Verellen, N.; Jeyaram, Y.; Silhanek, A. V.; Metlushko, V.; Ameloot, M.; Vandenbosch, G. A. E.; Moshchalkov, V. V. Volumetric Method of Moments and Conceptual Multilevel Building Blocks for Nanotopologies. *IEEE Photon. J.* **2012**, *4*, 267–282.
33. Gallinet, B.; Martin, O. J. F. Relation between Near-Field and Far-Field Properties of Plasmonic Fano Resonances. *Opt. Express* **2011**, *19*, 22167–22175.
34. López-Tejeira, F.; Paniagua-Domínguez, R.; Rodríguez-Oliveros, R.; Sánchez-Gil, J. A. Fano-like Interference of Plasmon Resonances at a Single Rod-Shaped Nanoantenna. *New J. Phys.* **2012**, *14*, 023035.
35. Verellen, N.; Van Dorpe, P.; Vercruysse, D.; Vandenbosch, G. A. E.; Moshchalkov, V. V. Dark and Bright Localized

Surface Plasmons in Nanocrosses. *Opt. Express* **2011**, *19*, 11034–11051.

36. Sonnefraud, Y.; Kerman, S.; Di Martino, G.; Lei, D. Y.; Maier, S. A. Directional Excitation of Surface Plasmon Polaritons *via* Nanoslits under Varied Incidence Observed Using Leakage Radiation Microscopy. *Opt. Express* **2012**, *20*, 4893–4902.